

Lawrence Berkeley National Laboratory

Recent Work

Title

Beyond a phenomenological description of magnetostriction.

Permalink

<https://escholarship.org/uc/item/1v83w246>

Journal

Nature communications, 9(1)

ISSN

2041-1723

Authors

Reid, AH
Shen, X
Maldonado, P
et al.

Publication Date

2018

DOI

10.1038/s41467-017-02730-7

Peer reviewed

ARTICLE

DOI: 10.1038/s41467-017-02730-7

OPEN

Beyond a phenomenological description of magnetostriction

A.H. Reid *et al.*[#] 

Magnetostriction, the strain induced by a change in magnetization, is a universal effect in magnetic materials. Owing to the difficulty in unraveling its microscopic origin, it has been largely treated phenomenologically. Here, we show how the source of magnetostriction—the underlying magnetoelastic stress—can be separated in the time domain, opening the door for an atomistic understanding. X-ray and electron diffraction are used to separate the sub-picosecond spin and lattice responses of FePt nanoparticles. Following excitation with a 50-fs laser pulse, time-resolved X-ray diffraction demonstrates that magnetic order is lost within the nanoparticles with a time constant of 146 fs. Ultrafast electron diffraction reveals that this demagnetization is followed by an anisotropic, three-dimensional lattice motion. Analysis of the size, speed, and symmetry of the lattice motion, together with *ab initio* calculations accounting for the stresses due to electrons and phonons, allow us to reveal the magnetoelastic stress generated by demagnetization.

. Correspondence and requests for materials should be addressed to A.H.R. (email: alexhmr@slac.stanford.edu) or H.A.Dür. (email: hermann.durr@physics.uu.se). [#]A full list of authors and their affiliations appears at the end of the paper.

The functional properties of materials often depend on the detailed and subtle interplay of electronic, spin and lattice degrees of freedom^{1–16}. The complexity of this interplay can lead to a variety of technologically useful behaviors. These effects include anomalous thermal expansion^{1,10,11}, optical switching of magnetization^{11–17}, and superconductivity¹⁸. Understanding the details of this electron–spin–lattice interplay remains one of the most challenging scientific problems in condensed matter physics. A particularly perplexing aspect is the strong coupling of magnetic spin to electron and lattice degrees of freedom observed in magnetically ordered metals. In such metals, spin order can be extinguished on a timescale of order of 100 fs^{4–8}. This fast timescale implies strong coupling of spin to the electronic system, seemingly not limited by the requirement of angular momentum conservation that necessitates the involvement of the lattice. This observation poses an interesting question, how strong or fast are the interactions that govern the spin–lattice effect of magnetostriction.

Iron platinum (FePt) alloys are a particularly rich example of materials that exhibit such electron–spin–lattice interplay. In the $L1_0$ crystal phase, FePt is ferromagnetically ordered with extremely high magnetocrystalline anisotropy, making FePt the material of choice for next-generation magnetic storage media^{19,20}. In addition, the FePt system displays magnetostriction, leading to anomalous thermal expansion with a c -axis contraction in the paramagnetic phase²¹. The anomalous thermal expansion leads to a temperature-dependent change in the tetragonal lattice distortion, a quantity that is instrumental for establishing the high magnetocrystalline anisotropy in FePt²². Recent reports have shown that FePt also exhibits an all-optical magnetization reversal when subjected to ultrashort pulses of circularly polarized optical light^{13,14}. However, the mechanism of how light switches magnetization in FePt is not yet understood. Therefore, understanding the interplay of electrons, spins, and lattice in FePt is a necessary step toward unraveling the mysteries of its rich functional properties.

Experimentally, lattice stress is not directly observable. Instead, measurements can be made of lattice strain—the physical movement of atoms in response to the stress. The strain response is often complex in solids where macroscopic effects can constrain the motion. For this reason, we choose nanoparticle grains of FePt held in a free-standing carbon matrix as the medium to understand the stress. Previous studies of magnetic structural dynamics were performed on continuous thin films deposited on

substrates^{23–25}. Our use of unconstrained FePt single-crystal nanoparticles allows us to study the full three-dimensional lattice motion on the natural timescale of the strain propagation through the nanoparticles^{26,27}. This approach separates the individual contributions from electrons, spins, and phonons to lattice stress in FePt particles via their different symmetry properties and temporal onsets, as illustrated in Fig. 1b. By employing *ab initio* calculations to capture the non-equilibrium stresses of electrons and phonons, we show that a large magnetoelastic stress term related to magnetostrictive spin–lattice coupling must contribute to the observed strain³. This term dominates the anomalous lattice expansion of FePt under the non-equilibrium condition during the first few ps following fs laser excitation.

Results

Spin and lattice response of FePt nanoparticles. In Fig. 1a, we show a TEM image of the free-standing sheet of FePt nanoparticles embedded in carbon, which is used in this study. The FePt nanoparticles are approximately cylindrically shaped with large surfaces that are free to respond to dynamic stresses along the surface normal. The particles are grown to have their magnetic easy axis, the crystallographic c -axis, along the surface normal (see “Methods” section). We expect that a linear stress–strain surface response will dominate the motion for a time of $\tau = r_{\text{np}}/v_s$, where r_{np} is the nanoparticle radius (mean $r_{\text{np}} = 6.5$ nm) and v_s is the speed of sound. A value of $\tau \approx 3$ ps is estimated for these FePt nanoparticles using the FePt sound velocity of 2.2 nm/ps²².

We measured the spin and lattice responses separately on the same FePt–C samples (see “Methods” section), although using different experimental setups. Figure 2 shows the spin and lattice responses of a free-standing layer of FePt nanoparticles to fs laser excitation. We measured the spin response with ultrafast X-ray resonant diffraction at the Fe L_3 -edge using circularly polarized X-rays¹⁵. Figure 2b shows the measured Fe spin response following fs laser excitation (see schematic in Fig. 2a and “Methods” section). The data shown in Fig. 2b are the difference of two measurements of the resonant X-ray diffraction intensity with the sample magnetized in opposite directions by applying an external magnetic field of ± 0.4 T during the experiment. This field strength is significantly lower than the field required to switch the FePt nanoparticles when no laser pump is applied; the switching field without laser pump at room temperature is

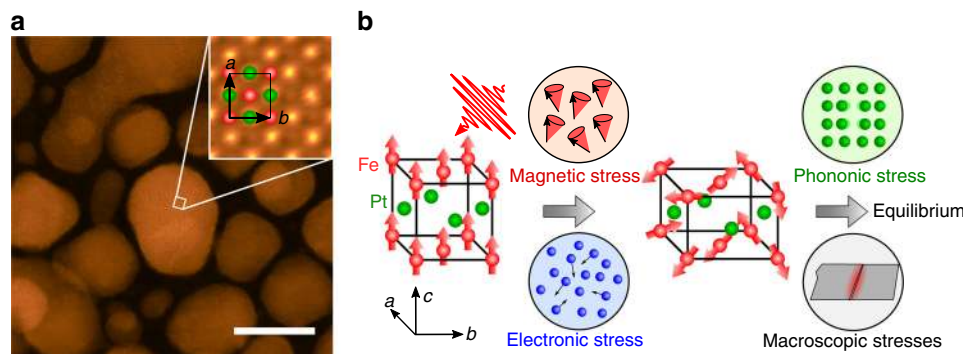


Fig. 1 FePt physical structure and the time sequences of contributions to the lattice strain. **a** High-angle annular dark-field scanning transmission electron microscopy images of the morphology and a -, b -plane atomic arrangement (inset) for FePt nanoparticles embedded in an amorphous carbon matrix. 10 nm scale bar shown in lower right. **b** The FePt crystal structure and magnetic arrangement. Fe and Pt atomic positions in the $L1_0$ lattice structure are indicated by red and green spheres in the insets, respectively. The majority of the grains are aligned with the a and b unit cells directions in the plane of the film. The schematic shows the sequence of stress contributions in FePt. In the first picosecond after laser excitation, the lattice is subject to the rapidly developing magnetic and electric stresses. This leads to an increase in the tetragonal distortion of the unit cell as illustrated. On a timescale of a few picoseconds, phonon and macroscopic stresses become important and the lattice moves toward its equilibrium state

measured to be $\pm 4 \text{ T}^{28}$. The large reduction of the switching field indicates that the magnetocrystalline anisotropy barrier between opposite magnetization directions is strongly reduced by laser excitation. The data in Fig. 2b are fitted with a double exponential⁶, resulting in a time constant for demagnetization of $146 \pm 15 \text{ fs}$, and a time constant of $16 \pm 4 \text{ ps}$ for the subsequent magnetization recovery. These results agree with optical fs laser experiments reported earlier^{6,7}. The fitted demagnetization amplitudes vs. laser pump fluence are shown in the inset of Fig. 2b.

We use ultrafast electron diffraction (UED) to directly measure the FePt nanoparticles' lattice response^{29,30}. The nanoparticles were crystallographically aligned from their growth on a single-crystal substrate; the substrate was subsequently removed (see "Methods" section). Therefore, the FePt diffraction pattern, shown in Fig. 2c, shows well-defined Bragg peaks. From time-resolved measurements of multiple Bragg diffraction peaks, the temporal evolutions of FePt lattice spacings along the *a* and *c* directions (the *b* direction evolves identically to the *a* direction) are extracted and shown as a function of time in Fig. 2d (see "Methods" section for details). We used a pump fluence of $5 \text{ mJ}/\text{cm}^2$ that corresponding to a fs demagnetization of 30% of the initial magnetization (see inset of Fig. 2b). The measured change in lattice spacing along the *c* direction is clearly different from the

change along the *a*- and *b*-lattice directions. The lattice spacing in the *a* and *b* directions of FePt shows a rapid expansion, which peaks at $\sim 3 \text{ ps}$. The expansion is followed by an oscillatory motion. The dynamics along the *c* direction is very different. The *c*-lattice spacing shows a rapid initial contraction on a similar timescale to the *a*- and *b*-lattice expansions. This *c*-lattice motion also oscillates anti-phase to the *a* and *b* directions. It then relaxes back toward the pre-excitation value on a timescale of $\sim 20 \text{ ps}$, whereas this does not occur in the *a* and *b* directions which show expansion.

Discussion

We are interested in understanding the dynamic response of the FePt lattice to the initial stresses generated during fs heating and demagnetization. To better visualize this initial lattice response, we replotted the FePt nanoparticle's unit cell volume and its *c*-*a* lattice vectors for two laser fluences in Fig. 3. The non-equilibrium state of the system is modeled using thermal baths for the occurring degrees of freedom of the nanoparticle. To this end, we extend the three-temperature model of FePt³¹, to include a temperature representing the carbon matrix (see "Methods" section). The four-temperature model results are shown in Fig. 3a. The temporal evolution of the unit cell volume, $V(t) = c(t)$.

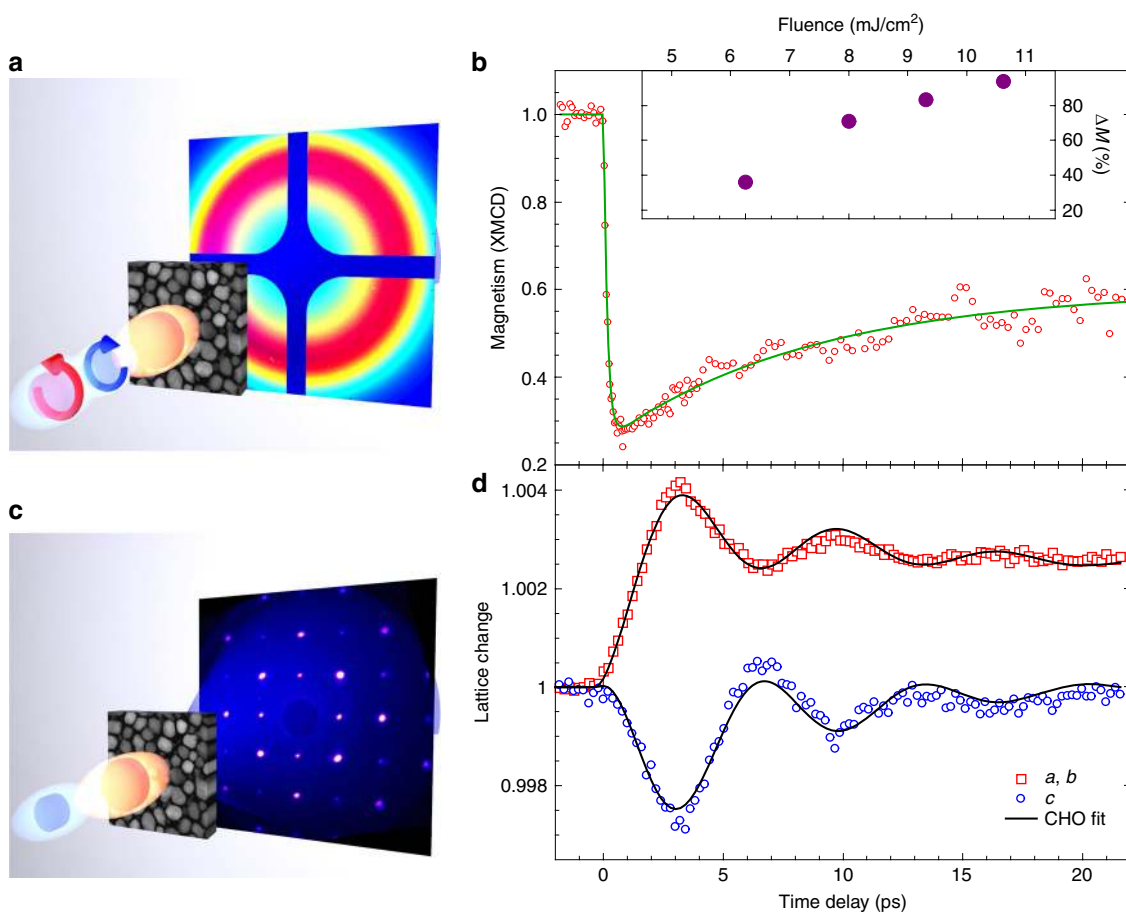


Fig. 2 Ultrafast spin and lattice dynamics of the FePt nanoparticles. **a** Experimental setup for time-resolved soft X-ray scattering measurements of the FePt magnetization dynamics. **b** The measured change in magnetization for a laser pump fluence of $9.5 \text{ mJ}/\text{cm}^2$. The solid line is a two-exponential fit to the data showing a $146 \pm 15 \text{ fs}$ drop followed by a $16 \pm 4 \text{ ps}$ recovery of the magnetization. The inset shows the size of the magnetization drop vs. pump fluence. **c** Experimental setup for ultrafast electron diffraction measurements of the time-resolved structural response of the FePt nanoparticles. **d** Measurements of the Bragg diffraction are used to determine the temporal evolution of the *a*-, *b*-lattice (red squares) and *c*-lattice (blue circles) spacings for a pump laser fluence of $5.0 \text{ mJ}/\text{cm}^2$. The solid lines are fits of a simple driven coupled harmonic oscillator (CHO) model to the data as described in the text

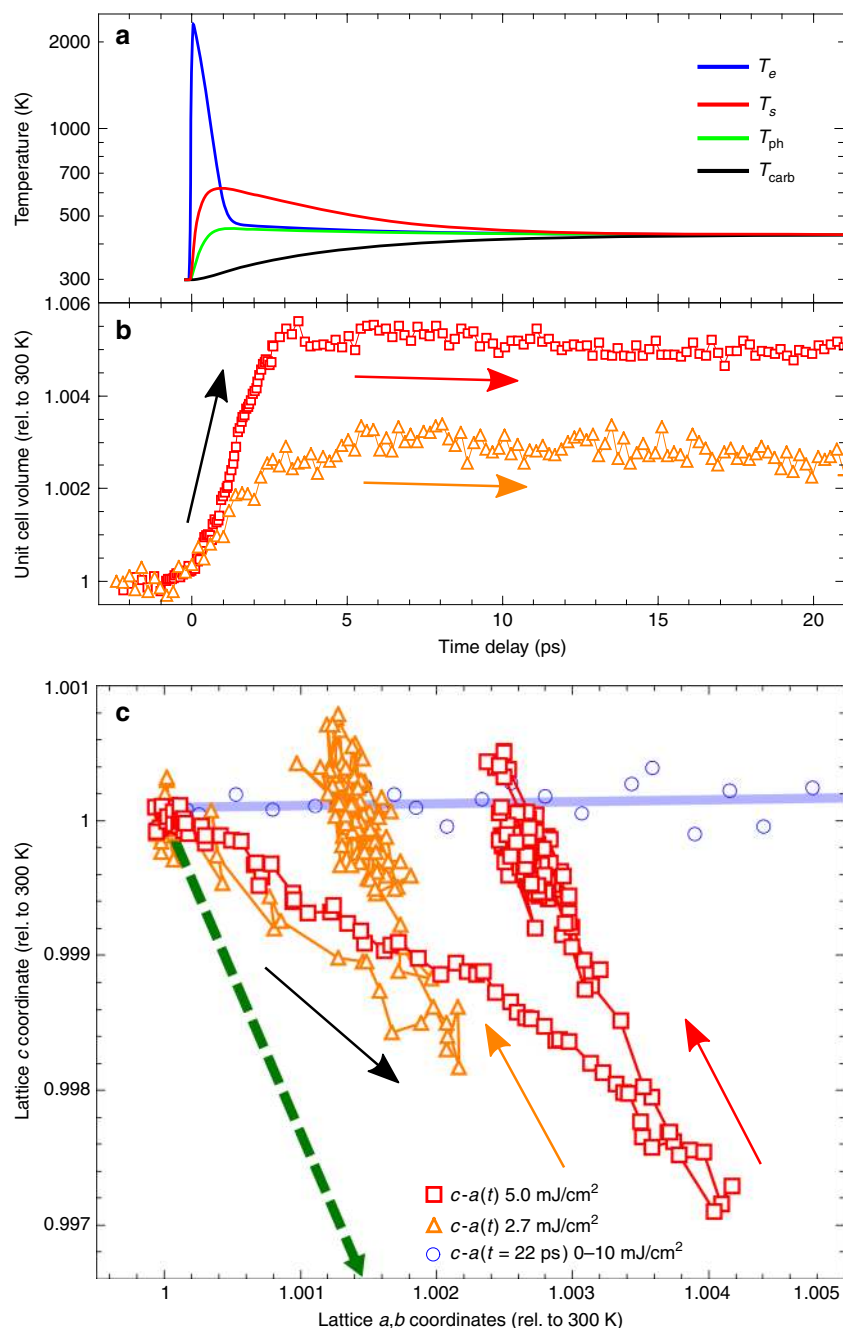


Fig. 3 The evolution of FePt's subsystems as a function of time. **a** An extended three-temperature model of electronic, spin, and lattice temperature evolution in FePt, together with the lattice temperature of the carbon matrix upon pumping with a laser fluence of 5.0 mJ/cm². **b** The temporal evolution of the unit cell volume ($V = c \cdot a^2$) calculated from the a and c lattice data at laser fluences of 5.0 mJ/cm² (red) and 2.7 mJ/cm² (orange). **c** The FePt lattice motion plotted as a relative change in the c - a plane, with arrows indicating the time direction. Quasi-equilibrium measurements of the nanoparticle thermal expansion as a function of laser fluence, made at a time delay of 22 ps, are shown as blue open circles. The dashed green arrow indicates the direction of the a - and c -lattice evolution corresponding to the calculated change between FM and PM ground states

$a(t)^2$ (note that $a(t) = b(t)$), is shown in Fig. 3b. This volume evolution shows that there is a clear cross-over from rapidly increasing volume to a steady-state regime at around 3 ps; this cross-over coincides with the first extremum of the oscillation in Fig. 2d. The 3 ps cross-over can also be identified as the turning point of the a - c trajectory plot in Fig. 3b, which displays the relative lattice change in the a - c plane. The characteristic motions are clearly separated. Initially, the lattice system moves along a trajectory defined by the stresses at the nanoparticle surfaces toward a turning point at 3 ps time delay. This delay is defined by the time taken for the strain waves to reach the center of the

nanoparticles. Following this time delay, the nanoparticles begin a damped ringing motion that brings them back to the quasi-equilibrium state for c - a thermal expansion (shown in blue as a function of laser fluence in Fig. 3b).

To understand the initial expansion trajectory in Fig. 3b, we conducted *ab initio* calculations of the electron and phonon stress contributions^{32,33}. The electronic stress σ^e is evaluated from a calculation of the electronic Grüneisen parameter along different symmetry directions (see “Methods” section). We determined that the electronic stress is anisotropic with $\sigma_{a,b}^e = 2\sigma_c^e$, but has a positive electronic pressure along all crystallographic axes. Next,

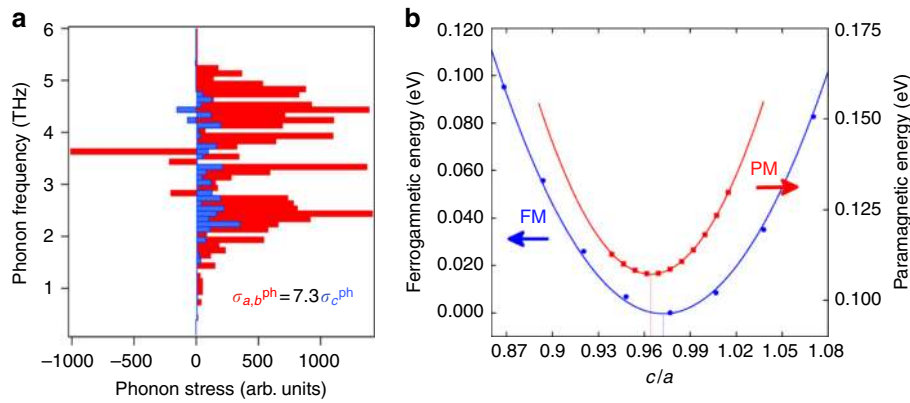


Fig. 4 Ab initio calculations of the lattice and magnetic stress. **a** The mode resolved lattice stress, σ_i^{ph} , along lattice directions, $i = a$ and c , calculated ab initio for a non-equilibrium phonon population. **b** The ab initio calculated total energies vs. c/a ratio for FePt in the ferromagnetic (FM, blue circles) and paramagnetic (PM, red circles) phase at constant volume. Calculations in the full a - and c -plane (not shown) determine the lattice parameters change to $\Delta a/a = +0.25\%$ and $\Delta c/c = -0.53\%$ when moving from the global energy minimum (not shown) of the ferromagnetic to the paramagnetic phase. We note that the calculated ferromagnetic ground-state value of $c/a = 0.964$ is in good agreement with $c/a = 0.972 \pm 0.003$ measured at room temperature (see Supplementary Figure 3c)

to treat the phonon stress contribution, we calculated the out-of-equilibrium behavior of the lattice from the phonon populations, assuming independent phonon modes and including phonon–phonon interactions (see “Methods” section). By UED measurement of the Debye–Waller effect, we experimentally determine that these modes are populated exponentially with a time constant of 2.7 ps³⁴. The ab initio calculated mode-dependent contributions to the phonon stress are shown in Fig. 4a. As with the electronic stress, we find that the non-equilibrium phonon stress is highly anisotropic with $\sigma_{a,b}^{\text{ph}} = 7.3\sigma_c^{\text{ph}}$, but it remains positive for all crystallographic directions. Consequently, to explain the strong negative strain observed along the c -axis, a further stress contribution arising from the magnetic system must be considered.

Any ab initio calculation of the magnetic stress relies on the details of the coupling between spins and lattice, and, spins and electrons. For ultrafast demagnetization, these details remain unknown. Instead, we attempt a more robust approach. We determine the structural ground state of FePt in the ferromagnetic (FM) and paramagnetic (PM) phases using spin-polarized density functional theory in the local density approximation (see “Methods” section for details). The calculated total energies for constant volume are shown as a function of the c/a ratio in Fig. 4b, and are in good agreement with the experimental values. The difference between the two structural energy minima for FM and PM phases are characterized by a -0.53% c -lattice contraction and $+0.25\%$ a -lattice expansion. It is assumed that the magnetic stress vector is characterized by a straight-line trajectory between these two phases, i.e., $\sigma_{a,b}^m \approx -0.47\sigma_c^m$. This stress trajectory is represented by the green arrow in Fig. 3c, and shows the required negative stress along the c -axis. We note that this would be the trajectory predicted for a 100% demagnetization, under static equilibrium conditions, and in our experiment we have neither 100% demagnetization nor equilibrium conditions.

To understand the relative sizes of the different stress contributions in the experiment, we can consider the FePt lattice response in terms of a simple coupled harmonic oscillator with a two-dimensional displacement coordinate: Q_i ($i = a, c$)³⁵. The lattice motion in Fig. 2d is modeled by:

$$\frac{d^2 Q_i}{dt^2} + 2\beta \frac{dQ_i}{dt} + \sum_j \Lambda_{ij} Q_j = \sigma_i(t), \quad (1)$$

where β is a phenomenological damping constant and, Λ_{ij} is a

matrix whose diagonal terms describe the frequency, ω , of the coherent breathing mode, while its off-diagonal terms represent the elastic coupling between $j = ab, c$ -lattice strains. Equation (1) is characterized by two solutions, with symmetric ($Q_{a,b} \sim Q_c$) and antisymmetric ($Q_{a,b} \sim -Q_c$) eigenvectors and eigenfrequencies $\omega_1 = \pm(\Lambda_{aa} + 2\Lambda_{ac})^{1/2}$ and $\omega_2 = \pm(\Lambda_{aa})^{1/2}$, respectively (we assume here that $\Lambda_{aa} = \Lambda_{cc}$). Figure 2d shows that the antisymmetric solution is favored. We note that the symmetry of the resulting lattice strain amplitude will depend on the symmetry of the driving stress terms as previously discussed. We describe the driving stresses in Eq. (1) as:

$$\sigma_{a,b}(t) = \sigma_{a,b}^e + \sigma_{a,b}^m + \sigma_{a,b}^{\text{ph}} + \sigma_{a,b}^{\text{carb}}, \quad (2)$$

$$\sigma_c(t) = \sigma_c^e + \sigma_c^m + \sigma_c^{\text{ph}}. \quad (3)$$

In the following paragraphs, we detail the form of the stresses assumed in the harmonic oscillator model

As discussed in the “Methods” section, the electronic stress σ_i^e is determined by the electronic temperature and electronic heat capacity of the system: $\sigma_i^e = -\gamma_i^e C_e(T_e) \delta T_e$. The transient electronic temperature is determined by the four-temperature model, while our ab initio electronic structure calculations determine the ratio of the coefficients to be: $\gamma_{ab} = 2\gamma_c$. The stress thus has the form: $\sigma_i^e = \sigma^e (\overleftarrow{ab} + 0.5\overleftarrow{c}) T_e(t) \delta T_e(t)$. A single scaling constant, σ^e , is used to characterize the transient electronic stress.

The magnetic stress, σ_i^m , is predicted by our FM and PM structural-ground-state calculations to have the trajectory $2.12\sigma_{ab}^m = -\sigma_c^m$. We assume this to be the case, and, further, assume that the stress must be proportional to the square of the change in magnetization, due to time reversal symmetry. Therefore, the evolution of this stress, is determined by the measured change in the FePt magnetization, having the form: $\sigma_i^m = \sigma^m (0.47\overleftarrow{ab} - \overleftarrow{c}) (\Delta M(t)/M_0)^2$, where $M(t)$ is defined by the bi-exponential fit to Fig. 2a. Again, a single parameter, σ^m , is used to characterize the strength of this stress component.

The stresses due to phonons are dominated by the low-energy modes due to the larger atomic displacement per unit energy associated with these modes. For this reason, the phonon stress is not adequately modeled by the lattice temperature—a measure of the energy in the lattice—but must also account for the phonon thermalization time. The attenuation of the Bragg reflections due to the Debye–Waller effect is measured to determine a lattice

Table 1 Parameters determined from fitting the coupled harmonic oscillator to the data in Fig. 2d

Stress	Equation/model	Fitting value	ab coefficient	c coefficient
σ^e	$\sigma^e T_e(t) \delta T_e(t)$	8.3e-10/ps ² /K ²	1	0.5
σ^{ph}	$\sigma^{ph} \left[1 - \exp\left(-\frac{t}{\tau_l}\right) \right]$	3.9e-3/ps ²	1	0.14
σ^m	$\sigma^m \left(\frac{\Delta M(t)}{M_0} \right)^2$	9.6e-3/ps ²	0.47	-1
σ^{carb}	$\sigma^{carb} T_{carb}(t)$	1.5e-5/ps ² /K	1	0

equilibration time. It is found that the mean-square atomic displacements increase with an exponential time constant τ_l of 2.7 ps. Again, we use our ab initio theory calculations to determine the relative strength of the phonon stresses in the *a*, *b* and *c* directions ($\sigma_{ab}^{ph} = 7.3\sigma_c^{ph}$). The phonon stress thus has the form: $\sigma_i^{ph} = \sigma^{ph} \left(\frac{\tau_{ab}}{ab} + 0.14 \frac{\tau_c}{c} \right) \left[1 - \exp\left(-\frac{t}{\tau_l}\right) \right]$.

Finally, we note that the carbon matrix must act to compress the nanoparticle in the *a*, *b* direction. The stress is assumed to evolve with the temperature of the carbon bath: $\sigma_{ab}^{carb} = \sigma^{carb} T_{carb}(t)$. No stress from the carbon is considered in the *c* direction, as nothing restrains the motion in this direction.

Using the above stress models, a least-squares non-linear curve fitting is made to the experimental data. The best fit to the experiment is shown in Fig. 2d. The form of these stresses present and the fitting values obtained are presented in Table 1. The results indicate that a non-zero magnetoelastic stress does develop within the FePt nanoparticle on the timescale of the ultrafast demagnetization. It is primarily this stress that drives in the anisotropic lattice displacement, which proceeds as a strain wave moving inwards from the nanoparticle's boundary.

Our results demonstrate how the stress contributions for different degrees of freedom can be separated in the time domain by measuring nanometer sized particles. In particular, we uncovered the existence of the magnetostrictive driving force for strongly anisotropic lattice motion in FePt nanoparticles. Magnetoelastic stress builds up on the sub-ps timescale, characteristic of ultrafast demagnetization. On the ps timescale, stress from transiently populated phonons takes over and results in a lattice tetragonal. Studies by Lukashev et al. have shown that a reduction in tetragonality favors a reduced FePt magnetocrystalline anisotropy barrier³⁶. We speculate that this reduced barrier results in reduced magnetic coercivity, which allows laser-excited FePt nanoparticles to reverse their magnetization in a magnetic field of 0.4 T. This observation provides a new avenue towards manipulating the magnetocrystalline anisotropy in future laser-assisted magnetic data storage technologies and opens the possibility of using this ultrafast magnetostriction for new types of THz frequency magnetostrictive actuators.

Methods

Sample preparation and characterization. The single crystalline L1₀ FePt grains were grown epitaxially onto a single-crystal MgO(001) substrate by co-sputtering Fe, Pt and C²⁸. This resulted in FePt nanoparticles of approximately cylindrical shape with heights of 10 nm and diameters in the range of 8–24 nm, with an average of 13 nm. The FePt nanoparticles form with *a* and *b* crystallographic directions oriented parallel to the MgO surface. The space in-between the nanoparticles is filled with glassy carbon, which makes up 30% of the film's volume. Following the sputtering process, the MgO substrate was chemically removed and the FePt-C films were floated onto copper wire mesh grids with 100- μ m-wide openings.

We performed electron diffraction from individual FePt nanoparticles using transmission electron microscopy (TEM). A high-resolution TEM image is shown in Fig. 1a. Supplementary Fig. 1a shows an FePt single-particle diffraction pattern. Fitting the peak shape, shown in Supplementary Fig. 1b, allows us to accurately determine the Bragg peak position. The room temperature equilibrium value of the tetragonal distortion is determined to be: $c/a = 0.972 \pm 0.003$. Diffraction patterns were taken at two sample temperatures, 300 K and 500 K, allowing us to measure

the static lattice expansion along *c*- and *a*-axes. The (400)-type Bragg peaks were used to probe the *a*-axis expansion. We deduce a +0.3% *a*-axis lattice expansion between 300 and 500 K. The determination of the *c*-axis lattice change is more difficult due to drifts of the sample positions at elevated temperatures. These data are plotted together with long-delay pump probe data in Supplementary Fig. 1c.

Resonant magnetic X-ray scattering from granular FePt. The dynamic magnetic response of the FePt nanoparticles to laser pulses of 50 fs duration and 800 nm central wavelength was measured at the SXR instrument of the Linac Coherent Light Source (LCLS) at SLAC. The average optical absorption of these nanoparticles was previously calculated to be 21%¹⁶. We probed the magnetization changes using circularly polarized X-rays, with the X-ray energy tuned to the Fe 2*p*–3*d* resonance (708 eV photon energy)¹⁵. Scattered X-rays were measured in transmission geometry by a pnCCD X-ray camera (illustrated in Fig. 2a). Radial scattering profiles, after azimuthal angular averaging of the pnCCD patterns, display a peak due to the interparticle scattering. Supplementary Fig. 2 shows typical radial scattering profiles after azimuthal angular averaging of the pnCCD patterns and the demagnetization time constants at individual wavevectors, *q*. The dashed (solid) lines in Supplementary Fig. 2b correspond to magnetic diffraction profiles obtained at positive (negative) pump probe time delays. The time constants for ultrafast demagnetization, shown in Supplementary Fig. 2a, were extracted from double exponential fits to the time delay traces at the respective wavevectors, *q*.

Figure 2b displays the difference in X-ray scattering yield with the sample magnetization aligned in externally applied magnetic fields of ± 0.4 T. This difference signal is proportional to the average particle magnetization along the X-ray incidence direction, switched by the external field. Note that 0.4 T is significantly lower than the static coercive field of 4 T in FePt nanoparticles, but allows a nearly 90% reversal of magnetization after laser excitation. We found that fs laser excitation, with the fluences shown in Fig. 2b, enabled a magnetization reversal similar to heat-assisted magnetic recording. We also measured the ultrafast magnetization dynamics of MgO supported FePt nanoparticles and found identical results to the free-standing FePt granular films shown in Fig. 2b.

Separating *c*-axis and *a*-, *b*-axis motion in UED data. The dynamic response of the FePt lattice was measured by ultrafast electron diffraction in a transmission geometry with 3 MeV electrons from the SLAC ultrafast electron diffraction source³⁰. The FePt nanoparticles were dynamically heated with a 1.55 eV, 50 fs optical laser pulse. To meet the Bragg condition for different lattice reflections, the film was rotated around axes normal to the probe beam. Due to geometrical restrictions, rotation angles were limited to 45° from normal incidence. Measurements were made at different incidence angles to access Bragg peaks with projections along the *c*-axis; these data are displayed in Supplementary Fig. 3. The time evolution data for Bragg peak positions (*hkl*) shows large differences for peaks with different “*l*” indexes, i.e., different projections along the out-of-plane (*c*-axis) direction. Peaks with the same relative projection along the *c*-axis, $l^2/(h^2+k^2+l^2)$, showed the same temporal response. Measurements of multiple Bragg reflections with different *c*-axis projections were used to extrapolate the motion along the *c*-axis (Supplementary Fig. 3b). The extrapolated motion for the FePt *c*-axis is shown in Fig. 2d, together with the directly measured *a*-axis (& *b*) motion.

Ab initio calculations of electronic and phononic stress. The ultrafast laser excitation of the FePt nanoparticles is followed by a dynamical response of the lattice, which can be characterized by magnetic, electronic and phononic stresses. To achieve a complete determination of the latter two, we used classical kinetic theory along with the Fermi's golden rule of scattering theory to derive novel out-of-equilibrium rate equations for the electronic and phononic distributions³⁷. We solve those equations by using input from first-principles calculations, where the incorporation of a temperature- and mode-dependent electron-phonon coupling and anharmonicities through phonon–phonon interaction are essential to attain a full solution of the time evolution.

The electron-phonon coupling was computed as response function within the density functional perturbation theory. We used a $16 \times 16 \times 16$ *k*-point grid in the Brillouin zone (BZ) for the self-consistent calculations and a $4 \times 4 \times 4$ grid for the phonon properties. Supplementary Fig. 4 shows the calculated mode-dependent phonon lifetimes due to electron-phonon coupling along high-symmetry lines in the BZ. We can observe that the smallest lifetimes correspond to the optical

Table 2 Model parameters used for the four-temperature model

Bath\Parameter	C_p (J/mol/K)	Coupling (10^{18} W/m ³ /K)	Excitation energy (J)
FePt electronic	$C_e = (4.0e-3)T_e$	$g_{es} = 0.08$ $g_{eph} = 0.7$	$5e-4$ (5 mJ/cm ²)
FePt spin	$C_s(300\text{ K}) = 1.5$ $C_s(600\text{ K}) = 4.1$ $C_s(700\text{ K}) = 10.6$ $C_s(750\text{ K}) = 34.7$ $C_s(755\text{ K}) = 0.3$	$g_{es} = 0.08$	—
FePt phonon	$C_{ph} = 71.4$	$g_{eph} = 0.7$ $g_{phc} = 1.6$	—
Carbon matrix	$C_{carb} = 8.5$	$g_{phc} = 1.6$	—

phonon modes, while, the lifetime of acoustic phonon modes increases exponentially for k -points approaching the Γ point. The computed lifetimes are used to describe the energy rate flowing from the electronic subsystem to the lattice after laser excitation; thus, they are needed to achieve a dynamical description of the system.

Subsequently, we obtained the induced stresses directly from the ab initio phononic and electronic distributions via a proportionality relation. We determined the contribution along the different real-space directions by the mode and branch dependence of the Grüneisen parameter and the phononic distribution.

Calculations of the phonon–phonon interaction. The phonon linewidths due to phonon–phonon interaction were determined using many-body perturbation theory in a third-order anharmonic Hamiltonian, which included up to three-phonon scatterings³⁸. Under these conditions, the phonon linewidth computation reduces to knowing the third-order anharmonic interatomic force constants, which can be determined from density functional theory calculations. To obtain the anharmonic phonon properties, we performed calculations with the finite displacement method using the PHONOPY package³⁹, with ABINIT employed as the ab initio code to calculate the pairwise and cubic interatomic force constants. To evaluate these, we employed supercells consisting of $4 \times 4 \times 4$ (128 atoms) and $3 \times 3 \times 3$ (54 atoms) primitive cells, respectively. Due to the high symmetry of the tetragonal system, only 4 and 316 sets of frozen phonon structures were needed to calculate the dynamical matrices and the phonon linewidths. During post processing, the phonon frequencies and lifetime were sampled on a $100 \times 100 \times 100$ q -mesh. Calculated phonon lifetimes were typically larger than several ps.

Supplementary Fig. 5 shows the calculated mode-dependent inverse phonon–phonon lifetimes as a function of the phonon frequency, along with an average inverse lifetime. From this plot, we can see that the phonon lifetimes for low-energy modes are of the order of 20 ps or larger, while only for LO modes the lifetimes are of the order of 10 ps or smaller. This calculation not only emphasizes the relatively short lifetime of the excited optical modes, which relax rapidly through decay into acoustic modes, it also provides us with quantitative, physical insights into the phonon thermalization process.

Electronic and phononic stresses. Instantaneous changes in the electron and phonon populations induced by a laser pulse or any other interaction induce a stress in the material leading, in the case of equilibrium distributions, to thermal expansion of the material. Microscopically, the induced stress can be written as:

$$\sigma = - \sum_k \gamma_e E_k \delta n_e - \sum_k \gamma_L(k) \hbar \omega_k \delta n_L(k), \quad (4)$$

where n_e and n_L are the electron and phonon populations, respectively, E_k and $\hbar \omega_k$ are the k -dependent electron and phonon energies and γ_e and $\gamma_L(k)$ are the corresponding electronic and phononic Grüneisen parameters, respectively⁴⁰.

Assuming that femtosecond electron–electron scatterings keep the electron distribution in a pseudo-equilibrium state, we can assess the thermal pressure due to excited conduction electrons by considering the electronic stress,

$$\sigma^e = -\gamma_e C_e \delta T_e, \quad (5)$$

where C_e is the specific heat capacity (per unit volume) of the electronic system with temperature T_e . Thermal effects can be taken into account⁴¹, and the specific heat and electronic Grüneisen parameter can be computed. Since the specific heat can be assumed to be isotropic, it is the electronic Grüneisen parameter that determines the anisotropic behavior of the electronic stress. To determine the anisotropic behavior, we have calculated the electronic Grüneisen parameter along different symmetry directions using the equation:

$$\gamma_e = \left(\frac{\partial \ln g(E_F)}{\partial \ln V} \right)_T, \quad (6)$$

where $g(E_F)$ is the electronic density of states.

Having calculated the electronic Grüneisen parameter along the c - and the a -axis, we find that its value along the a -axis is a factor ~ 2 larger than along the c -axis

(2.59 against 1.40). From these results, we infer that the electronic Grüneisen parameter has a non-negligible contribution along the c -axis and that a positive electronic thermal pressure along all crystallographic directions is expected.

For the lattice system, we compute the temporal and spatial evolution of the phonon population with a state-of-the-art methodology that goes beyond the conventional two-temperature model. Here, the out-of-equilibrium behavior of the lattice system is correctly treated by assuming independent phonon modes and by including the phonon–phonon interaction. In this manner, the mode-dependent lattice stress can be computed for non-equilibrium phonon populations, giving the results shown in Fig. 4a. Here it is important to emphasize that the phonon stress has been calculated for all real-space directions, but only the projections along the a - and c -axis have been plotted. In addition, and to weight the contribution of the different strain waves, only strain waves with group velocities larger than 1000 m/s have been considered. The large anisotropy in the phononic system shown in Fig. 4a (phonon stress along the a -axis being seven times larger than the phonon stress along the c -axis) has its origin in the combination of two main quantities. The first one is the large anisotropy of the Grüneisen parameter for phonon modes with group velocity larger than 1000 m/s, and the second one is the different change in phonon population for different modes. Thus, we find that phonon modes propagating along the c -axis either have a small Grüneisen parameter, a small change in the phonon population or very small group velocities, and would therefore not contribute to the lattice expansion at short timescales.

Ab initio calculations of FePt ground-state properties. The ground-state properties of ferromagnetic FePt have been calculated using spin-polarized density functional theory (DFT) in the local density approximation (LDA) as implemented in the code ABINIT⁴².

The electron–ionic core interaction on the valence electrons was represented by projector-augmented wave potentials (PAW)⁴³, and the wave functions were expanded in plane waves with an energy cutoff at 29 Hartree and a cutoff for the double grid of 31 Hartree, which was sufficient to converge the total energy for a dense k -point sampling. Reciprocal space sampling was performed using the Monkhorst-Pack scheme with a k -point mesh of $32 \times 32 \times 32$. After optimization, the lattice parameters for the FePt L1₀ (P4/mmm) structure were found to be $a = 3.857$ Å and $c = 3.761$ Å, which is comparable to the experimental values $a = 3.852$ Å and $c = 3.713$ Å. The resulting value of $c/a = 0.975$ is in good agreement with experiment ($c/a = 0.964$). The local magnetic moments of the Fe atoms in the ordered FePt structures in the ferromagnetic phase are 3.065 μ_B .

For the paramagnetic (PM) state, we adopt the disordered local moments (DLM) approach, which states that paramagnetism can be modeled as a state where atomic magnetic moments are randomly oriented (i.e., non-collinear magnetism). The DLM approach can be simplified by considering only collinear magnetic moments when the spin-orbit coupling is not taken into account. Hence, the problem of modeling paramagnetism becomes a problem of modeling random distributions of collinear spin components. It can be solved by using special quasi-random structures (SQS). A SQS is a specially designed supercell built of ideal lattice sites to mimic the most relevant pair and multisite correlation functions of a completely disordered phase (PM order in our case). As PM simulation cell, we adopted an extended lattice cell of 32 atoms (16 FePt unit cells). The disordered local moment approach (or SQS) provides a better description of the PM phase than the spin-non-polarized calculation, even without SOC, and gives good results for magnetostriction (even without SO)⁴⁴.

The thus-calculated PM phase shows an expansion of 0.25% in the a, b -direction and a reduction of -0.53% in the c -lattice direction when moving from the ferromagnetic to the paramagnetic phase. Thus, the computed c/a -ratio of paramagnetic FePt becomes 0.964. The expected change in the lattice constants between the FM and PM phases under static conditions is indicated by the dashed green arrow in Fig. 3c.

Four-temperature model of non-equilibrium state. The microscopic three-temperature model (M3TM) has been developed to understand the nature and evolution of the non-equilibrium state in laser-excited ferromagnets⁴⁵. This model has been recently applied to FePt:Cu by Kimling et al.³¹. Here we adapt the model of Kimling et al. to our sample of FePt nanoparticles in a carbon matrix. We model the system as four coupled thermal baths: the FePt electronic bath; the FePt spin

bath; the FePt phonon bath, and the carbon matrix bath. Each bath has its own associated temperature. Table 2 summarizes the parameters used in the model, the heat capacities of the four baths and relative coupling strengths between the baths. We note that the phonon bath is approximated by a constant heat capacity over the modeled range for simplicity; this is justified by a Debye model of C_{ph} , which suggests that only a negligible 3% change heat capacity would occur in this range. The four equations of the model are:

$$C_e \frac{dT_e}{dt} = g_{eph}(T_{ph} - T_e) + g_{es}(T_s - T_e), \quad (7)$$

$$C_{ph} \frac{dT_{ph}}{dt} = g_{eph}(T_e - T_{ph}) + g_{phc}(T_{carb} - T_{ph}), \quad (8)$$

$$C_s \frac{dT_s}{dt} = g_{es}(T_e - T_s), \quad (9)$$

$$C_{carb} \frac{dT_{carb}}{dt} = g_{phc}(T_{ph} - T_{carb}). \quad (10)$$

The model is solved numerically for an excitation of the electronic temperature with a duration of 50 fs. The solution obtained is shown in Fig. 3a.

Data availability. The authors declare that the data supporting the findings of this study are available within the article and its Supplementary Information files. All other relevant data supporting the findings of this study are available on request.

Received: 2 December 2016 Accepted: 19 December 2017

Published online: 26 January 2018

References

- del Moral, A. *Handbook of Magnetism and Advanced Magnetic Materials. Magnetostriction and Magnetoelasticity Theory: A Modern View* (John Wiley & Sons, Ltd, Hoboken NJ, 2007).
- Pascarelli, S. et al. 4f change-density deformation and magnetostrictive bond strain observed in amorphous TbFe₂ by x-ray absorption spectroscopy. *Phys. Rev. B* **81**, 020406 (2010).
- Filippetti, A. & Hill, N. A. Magnetic stress as a driving force of structural distortions: the case of CrN. *Phys. Rev. Lett.* **85**, 5166–5169 (2000).
- Beaurepaire, E., Merle, J.-C., Daunois, A. & Bigot, J.-Y. Ultrafast spin dynamics in ferromagnetic nickel. *Phys. Rev. Lett.* **76**, 4250 (1996).
- Stamm, C. et al. Femtosecond modification of electron localization and transfer of angular momentum in nickel. *Nat. Mater.* **6**, 740 (2007).
- Mendil, J. et al. Resolving the role of femtosecond heated electrons in ultrafast spin dynamics. *Sci. Rep.* **4**, 3980 (2014).
- Iihama, S. et al. Ultrafast demagnetization of L1₀ FePt and FePd ordered alloys. *J. Phys. D Appl. Phys.* **49**, 035002 (2016).
- Rudolf, D. et al. Ultrafast magnetization enhancement in metallic multilayers driven by superdiffusive spin current. *Nat. Commun.* **3**, 1037 (2012).
- Liu, Z.-K., Wang, Y. & Shang, S.-L. Thermal expansion anomaly regulated by entropy. *Sci. Rep.* **4**, 7043 (2014).
- von Reppert, A. et al. Persistent non equilibrium dynamics of the thermal energies in the spin and phonon systems of an antiferromagnet. *Struct. Dyn.* **3**, 054302 (2016).
- Stanciu, C. D. et al. All-optical magnetic recording with circularly polarized light. *Phys. Rev. Lett.* **99**, 047601 (2007).
- Mangin, S. et al. Engineered materials for all-optical helicity-dependent magnetic switching. *Nat. Mater.* **13**, 286–292 (2014).
- Lambert, C.-H. et al. All-optical control of ferromagnetic thin films and nanostructures. *Science* **345**, 1337–1340 (2014).
- John, R. et al. Magnetization switching of FePt nanoparticle recording medium by femtosecond laser pulses. *Sci. Rep.* **7**, 4114 (2017).
- Graves, C. E. et al. Nanoscale spin reversal by non-local angular momentum transfer following ultrafast laser excitation in ferromagnetic GdFeCo. *Nat. Mater.* **12**, 293–298 (2013).
- John, R. et al. Magnetisation switching of FePt nanoparticle recording medium by femtosecond laser pulses. *Sci. Rep.* **7**, 4114 (2017).
- Granitzka, P. W. et al. Magnetic switching in granular FePt layers promoted by near-field laser enhancement. *Nano. Lett.* **17**, 2426–2432 (2017).
- de Gennes, P. G. *Superconductivity of Metals and Alloys*. (W.A. Benjamin, Inc, New York, 1966).
- Weller, D., Mosendz, O., Parker, G., Pisana, S. & Santos, T. S. L1₀ FePt X-Y media for heat-assisted magnetic recording. *Phys. Status Solid A* **210**, 1245–1260 (2013).
- Giri, A., Hun Wee, S., Jain, S., Hellwig, O. & Hopkins, P. E. Influence of chemical ordering on the thermal conductivity and electronic relaxation in FePt thin films in heat assisted magnetic recording applications. *Sci. Rep.* **6**, 32077 (2016).
- Tsunoda, Y. & Kobayashi, H. Temperature variation of the tetragonality in ordered PtFe alloy. *J. Magn. Magn. Mater.* **272–276**, 776–777 (2004).
- Kanazawa, H., Lauhoff, G. & Suzuki, T. Magnetic and structural properties of (Co_xFe_{100-x})Pt₅₀ alloy thin films. *J. Appl. Phys.* **87**, 6143–6145 (2000).
- Jal, E. et al. Structural dynamics during laser-induced ultrafast demagnetization. *Phys. Rev. B* **95**, 184422 (2017).
- Xu, D. B. et al. Spatiotemporally separating electron and phonon thermal transport in L1₀ FePt films for heat assisted magnetic recording. *J. Appl. Phys.* **115**, 243907 (2014).
- Couet, S. et al. Anisotropic lattice dynamics of FePt L1₀ thin films. *Phys. Rev. B* **82**, 094109 (2010).
- Szilagyi, E. et al. Visualization of nanocrystal breathing modes at extreme strains. *Nat. Commun.* **6**, 6577 (2015).
- Clark, J. N. et al. Ultrafast three-dimensional imaging of lattice dynamics in individual gold nanocrystals. *Science* **341**, 56–59 (2013).
- Varaprasad, B. S. D. Ch. S., Wang, J., Shiroyama, T., Takahashi, Y. K. & Hono, K. Columnar structure in fept-c granular media for heat-assisted magnetic recording. *IEEE Trans. Magn.* **51**, 3200904 (2015).
- Wang, X. et al. Electronic Grüneisen parameter and thermal expansion in ferromagnetic transition metal. *Appl. Phys. Lett.* **92**, 121918 (2008).
- Weathersby, S. P. et al. Mega-electron-volt ultrafast electron diffraction at SLAC National Accelerator Laboratory. *Rev. Sci. Instrum.* **86**, 073702 (2015).
- Kimling, J. et al. Ultrafast demagnetization of FePt:Cu thin films and the role of heat capacity. *Phys. Rev. B* **90**, 224408 (2014).
- Carva, K., Battiato, M., Legut, D. & Oppeneer, P. M. *Ab initio* theory of electron-phonon mediated ultrafast spin relaxation of laser-excited hot electrons in transition-metal ferromagnets. *Phys. Rev. B* **87**, 184425 (2013).
- Henighan, T. et al. Generation mechanism of terahertz coherent acoustic phonons in Fe. *Phys. Rev. B* **93**, 220301 (2016).
- Chase, T. et al. Ultrafast electron diffraction from non-equilibrium phonons in femtosecond laser heated Au films. *Appl. Phys. Lett.* **108**, 041909 (2016).
- Wang, X. et al. Temperature dependence of electron-phonon thermalization and its correlation to ultrafast magnetism. *Phys. Rev. B* **81**, 220301 (2010).
- Lukashev, P. V., Horrell, N. & Sabirianov, R. F. Tailoring magnetocrystalline anisotropy of FePt by external strain. *J. Appl. Phys.* **111**, 07A318 (2012).
- Maldonado, P., Carva, K., Flammer, M. & Oppeneer, P. M. Theory of out-of-equilibrium ultrafast relaxation dynamics in metals. *Phys. Rev. B* **96**, 174439 (2017).
- Togo, A., Chaput, L. & Tanaka, I. Distributions of phonon lifetimes in Brillouin zones. *Phys. Rev. B* **91**, 094306 (2015).
- Togo, A. & Tanaka, I. First principles phonon calculations in material science. *Scr. Mater.* **108**, 1–5 (2015).
- Wright, O. B. Ultrafast nonequilibrium stress generation in gold and silver. *Phys. Rev. B* **49**, 9985 (1994).
- Boness, D. A., Brown, J. M. & McMahan, A. K. The electronic thermodynamics of iron under Earth core conditions. *Phys. Earth Planet Inter.* **42**, 227 (1986).
- Gonze, X. et al. ABINIT: First-principles approach to material and nanosystem properties. *Comp. Phys. Comm.* **180**, 2582–2615 (2009).
- Torrent, M., Jollet, F., Bottin, F., Zerah, G. & Gonze, X. Implementation of the projector augmented-wave method in the ABINIT code: Application to the study of iron under pressure. *Comp. Mat. Sci.* **42**, 337–351 (2008).
- Khmelevskiy, S., Turek, I. & Mohn, P. Spontaneous volume magnetostriction and non-Stoner behavior of the valence band in pure hcp Gd. *Phys. Rev. B* **70**, 132401 (2004).
- Koopmans, B. et al. Explaining the paradoxical diversity of ultrafast laser-induced demagnetization. *Nat. Mater.* **9**, 259–265 (2010).

Acknowledgements

P.M.K.C., and P.M.O. acknowledge support from the Swedish Research Council (VR), the Knut and Alice Wallenberg Foundation (grant No. 2015.0060), the Röntgen-Ångström Cluster, the European Union's Horizon 2020 Research and Innovation Programme under Grant agreement No. 737709 (FEMTOTERABYTE) and the Swedish National Infrastructure for Computing (SNIC).

Author contributions

A.H.R., H.A.D. conceived the experiment, Y.K.T., E.E.F., O.H. grew and characterized the samples, A.H.R., X.S., T.C., R.K.L., T.V., N.H., R.C., J.W., X.W., H.A.D. performed the electron diffraction experiments and analysis, A.H.R., E.J., T.C., P.G., T.L., Z.C., D.H., G.

D., W.F.S., H.O., J.S., H.A.D. performed the X-ray experiments and analysis, A.H.R., J.L., Y.Z., J.C. performed the simulations, P.M., K.C., P.O. performed ab initio calculations, A.H.R., H.A.D. coordinated writing of the paper with contributions from all coauthors.



Open Access This article is licensed under a Creative Commons Attribution 4.0 International License, which permits use, sharing, adaptation, distribution and reproduction in any medium or format, as long as you give appropriate credit to the original author(s) and the source, provide a link to the Creative Commons license, and indicate if changes were made. The images or other third party material in this article are included in the article's Creative Commons license, unless indicated otherwise in a credit line to the material. If material is not included in the article's Creative Commons license and your intended use is not permitted by statutory regulation or exceeds the permitted use, you will need to obtain permission directly from the copyright holder. To view a copy of this license, visit <http://creativecommons.org/licenses/by/4.0/>.

Additional information

Supplementary Information accompanies this paper at <https://doi.org/10.1038/s41467-017-02730-7>.

Competing interests: The authors declare no competing financial interests.

Reprints and permission information is available online at <http://npg.nature.com/reprintsandpermissions/>

Publisher's note: Springer Nature remains neutral with regard to jurisdictional claims in published maps and institutional affiliations.

© The Author(s) 2018

A.H. Reid^{1,2}, X. Shen³, P. Maldonado⁴, T. Chase^{1,5}, E. Jal^{1,6}, P.W. Granitzka^{1,7}, K. Carva⁸, R.K. Li³, J. Li⁹, L. Wu⁹, T. Vecchione³, T. Liu^{1,10}, Z. Chen^{1,10}, D.J. Higley^{1,5}, N. Hartmann², R. Coffee², J. Wu³, G.L. Dakovski², W.F. Schlotter², H. Ohldag¹¹, Y.K. Takahashi¹², V. Mehta^{13,14}, O. Hellwig^{13,15,16}, A. Fry², Y. Zhu⁹, J. Cao¹⁷, E.E. Fullerton¹⁸, J. Stöhr¹, P.M. Oppeneer⁴, X.J. Wang³ & H.A. Dürr^{1,4}

¹Stanford Institute for Materials and Energy Sciences, SLAC National Accelerator Laboratory, 2575 Sand Hill Road, Menlo Park, CA 94025, USA.

²Linac Coherent Light Source, SLAC National Accelerator Laboratory, 2575 Sand Hill Road, Menlo Park, CA 94025, USA. ³Accelerator Division, SLAC National Accelerator Laboratory, 2575 Sand Hill Road, Menlo Park, CA 94025, USA.

⁴Department of Physics and Astronomy, Uppsala University, P. O. Box 516, S-75120 Uppsala, Sweden. ⁵Department of Applied Physics, Stanford University, Stanford, CA 94305, USA.

⁶CNRS, Laboratoire de Chimie Physique - Matière et Rayonnement, Sorbonne Universités, UPMC Univ. Paris 06, 75005 Paris, France. ⁷Van der Waals-Zeeman Institute, University of Amsterdam, 1018XE Amsterdam, The Netherlands.

⁸Faculty of Mathematics and Physics, Department of Condensed Matter Physics, Charles University, Ke Karlovu 5, CZ-12116 Prague 2, Czech Republic. ⁹Brookhaven National Laboratory, Upton, NY 1193, USA.

¹⁰Department of Physics, Stanford University, Stanford, CA 94305, USA. ¹¹Stanford Synchrotron Radiation Laboratory, SLAC National Accelerator Laboratory, 2575 Sand Hill Road, Menlo Park, CA 94025, USA.

¹²Magnetic Materials Unit, National Institute for Materials Science, Tsukuba, 305-0047, Japan. ¹³San Jose Research Center, HGST a Western Digital Company, 3403 Yerba Buena Road, San Jose, CA 95135, USA.

¹⁴Thomas J. Watson Research Center, 1101 Kitchawan Road, Yorktown Heights, NY 10598, USA. ¹⁵Institute of Physics, Technische Universität Chemnitz, Reichenhainer Straße 70, D-09107 Chemnitz, Germany.

¹⁶Institute of Ion Beam Physics and Materials Research, Helmholtz-Zentrum Dresden-Rossendorf, 01328 Dresden, Germany. ¹⁷Department of Physics and National High Magnetic Field Laboratory, Florida State University, Tallahassee, FL 32310, USA.

¹⁸Center for Memory and Recording Research, UC San Diego, 9500 Gilman Drive, La Jolla, CA 92093-0401, USA